Energy Proceedings
Vol 50, 2025
ISSN 2004-2965

The influence mechanism of external electric field on the control of solid-liquid interface heat flux#

Xueling Liu [1,2], Yunkai Leng[1], Jia Hao[1], Jiansheng Wang[1*]

1 School of Mechanical Engineering, Tianjin University, Tianjin, 300350, P. R. China

2 Tianjin Geothermal Research & training Center, Tianjin University, Tianjin 300350, P. R. China
(Corresponding Author: jsw@tju.edu.cn)

ABSTRACT

In response to the problem of using cooling fluid to cool the bottom surface of components or devices, this study adds charged particles to the cooling fluid and regulates the heat flow by adjusting the electric field strength. In order to explore the microscopic mechanism of the effect of electric field strength on the heat transfer process in micro- and nano-fluidic channels, the convective heat transfer characteristics of argon fluid cooling on a platinum wall under different electric field strengths are simulated using the molecular dynamics method. A molecular dynamics (MD) model for the convective heat transfer of argon fluid in microchannels is established and the heat transfer process is simulated under different electric field strengths. The radial distribution functions (RDFs), vibrational density of states (VDOS) and atomic distribution functions of the atoms in the system are calculated, and the microscopic mechanism of convective heat transfer between argon fluid and platinum wall is analyzed. The influence of electric field intensity on the temperature and velocity distribution of the argon fluid is studied. The variation law of Nusselt number (Nu) and its controlling effect on the direction of the heat flow are analyzed. The results show that increasing the electric field intensity can improve the convective heat transfer characteristics in microchannels. Compared with no electric field, when the electric field intensity is 2.0V/nm, the *Nu* at the bottom and the top surfaces are increased by 42% and 56%, respectively. The temperature difference between the inlet and outlet is increased by 22.4%, the external temperature is reduced by 109.2K.

Keywords: Heat flow control, interface thermal resistance, flow heat transfer, electric field

NONMENCLATURE

Abbreviations	
MD	Molecular dynamics
RDFs	Radial distribution functions
VDOS	Vibrational density of states
FCC	Face center cubic
NEMD	Non-equilibrium molecular dynamics
EMD	Equilibrium molecular dynamics
Symbols	
E	Electric field intensity
A	Cross-sectional area
T	Temperature
C	Concentration
Nu	Nusselt number
$\phi(r_{ij})$	Potential function
ε	Potential function energy parameter
σ	Potential function distance parameter
Φ	Heat flux
τ	Shear stress
a_0	Lattice constant
$\AA$	Angstrom
k	Spring constant
Ar	Argon
Cu	Copper
O	Oxygen

1. INTRODUCTION

External surface heat dissipation techniques for devices aim to reduce the external surface temperature of the device by modulating the heat transfer characteristics of the target to improve the efficiency of heat transfer in a particular direction [1]. Conventional external surface heat dissipation techniques mainly involve coating the target surface with paint or covering a mesh structure to reduce the radiant energy of the target [2][3]. Currently, the main methods include phase-change thermal control [4], electro-variable temperature [5], thermogenic emissivity [6][7], dynamic regulation of electro-variable emissivity [8], and photonic crystals [9]. In addition, microfluidics as an emerging technology has

This is a paper for the 16th International Conference on Applied Energy (ICAE2024), Sep. 1-5, 2024, Niigata, Japan.

also been applied in external surface heat dissipation technology [10]. Remco [11] demonstrated an integrated microfluidic heat sink for cooling electronic devices. They mentioned that microchannel-based cooling technology can improve the cooling effect in chips by 50 times.

In addition, microchannel flow cooling technology has the advantages of high integration and easy packaging compared to traditional cooling means. In microchannels, as the scale gets smaller, the surface effect gradually becomes the main factor affecting the heat transfer process, and the thermal conductivity of the material itself also has an increasing effect on the heat transfer process.

Many scholars have carried out relevant studies on the heat transfer properties of solid-liquid interfaces: in 1941, Kapitza et al. [12] discovered the interfacial thermal resistance (ITR) of the solid-liquid helium interface, which is also known as the Kapitza thermal resistance. Barrat and Chiaruttini [13] used both non-equilibrium molecular dynamics (NEMD) and equilibrium molecular dynamics (EMD) simulations to calculate the Kapitza resistance of solid-liquid interfaces and found that both NEMD and EMD simulations show that the Kapitza resistance decreases monotonically as the strength of the interfacial interaction between solid and liquid atoms is increased from the non-wetting case to the wetting case. Xue et al. [14] also found two different mechanisms for the Kapitza thermal resistance through NEMD simulations. The trend of decreasing Kapitza thermal resistance with increasing interaction strength has also been found in the study of various solid-liquid interfaces [15]. In addition, Murad and Puri [16] investigated the temperature dependence of Kapitza thermal resistance at the Si/water interface using NEMD simulations. The Kapitza thermal resistance showed a decreasing trend with increasing temperature in liquid-gas coexistence phase, strict liquid phase and supercritical liquid phase. In addition, Ma et al. [17] found through NEMD simulations that attaching point charges to graphene sheets in a certain pattern can greatly reduce the Kapitza thermal resistance at graphene-water interfaces, which is partly due to the enhancement of solid-liquid interactions by Coulombic forces.

In this study, the effect of applied electric field on convective heat transfer at the solid-liquid interface is simulated by using a molecular dynamics model, and the results of the study will provide a guide to the enhanced heat transfer at the solid-liquid interface.

2. PHYSICAL MODEL AND NUMERICAL METHODS

2.1 Physical model

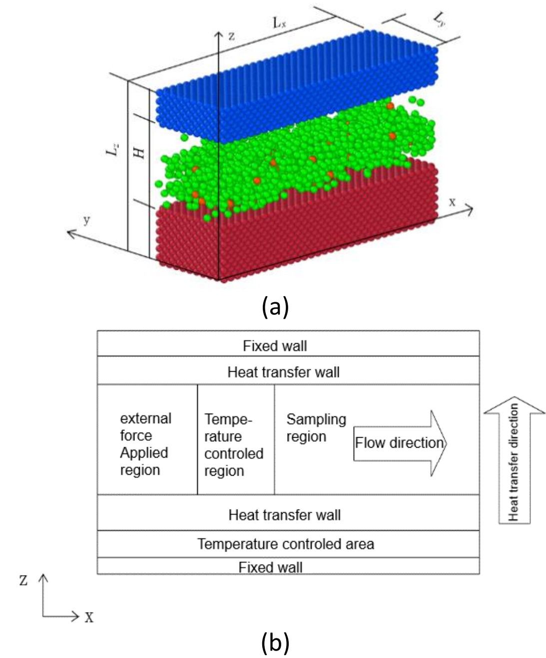

Fig. 1 Schematic diagram of nano-channel configurations as well as nanostructures (a)Modeling diagram of nanochannels (b) Partitioning of the simulation

For the convective cooling of platinum wall surfaces using argon fluid, a physical model is established as shown in Fig. 1(a), where the bottom surface is the hot wall surface of the equipment, i.e., the wall surface that needs to be cooled, and the top surface is the outer wall surface of the system, which is required to reduce the temperature difference between the outer wall surface of the system and the environment in a specific case. In this study, charged particles are added to the argon fluid, and the electric field strength is adjusted to achieve the regulation of the direction of heat flow. In order to study the effects of electric field strength on convective heat transfer, a molecular dynamics computational model of heat transfer of argon fluid flowing in a micro- and nanochannel is established, with the red area as the hot wall surface, the blue area as the cold wall surface, and the argon fluid in the middle part, in which the heterochromatic spheres are the charged particles. The platinum atoms on the solid wall surface are arranged in a face centered cubic (FCC) manner, with the lattice constant taking the value of a_0=4.04*Å*. The surfaces where the platinum atoms are in contact with the argon fluid are all set to be the (1,1,1) crystal surfaces of their cells. The charged particles added to the argon fluid have the same mass as the argon atoms, with a charge of±1*e*,

and the concentration of the charged particles is recorded as *C*.

Fig. 1(b) shows a schematic diagram of the relevant regions in the molecular dynamics simulation and calculation process. The fluid channel along the flow direction is divided into three regions: applied external force region, temperature control region, and data sampling region. The region $0<x<6a_0$ from the inlet of the channel is the applied external force region, where an external force *F* is applied to the fluid to drive the fluid flow, and the initial velocity of the fluid entering the sampling region can be changed by adjusting the magnitude of *F*. To ensure that the inlet temperature into the data sampling region is stabilized at a set temperature, the region $6a_0<x<12a_0$ along x-direction is set as the temperature-controlled region. The region along x-direction $12a_0<x<32a_0$ is the sampling region, which is the region where the fluid convectively exchanges heat with the wall, i.e. the region of the simulation study, and where the collection of relevant parameters takes place. The thermal wall surface is located at the bottom of the model, in order to simulate the need for calculation of the solid wall surface is divided into three layers: the bottom of a lattice constant within the height of $1a_0$ is set as a fixed layer of the model, the fixed layer above the height of the solid part of the temperature-controlled zone within the height of $2a_0$, the temperature-controlled layer above the height of the $3a_0$ within the range of the thermal wall surface of the heat transfer layer. The outer wall surface of the system is divided into two layers: the thickness of the heat transfer layer in contact with the fluid is $3a_0$, and the outer $1a_0$ is the fixed layer of the model. The role of the fixed layer is to maintain the shape of the model and prevent the model from drastic deformation during the simulation. The temperature control layer is used to maintain the temperature of the system. The Einstein wall model is used for both the top and bottom surfaces, which applies a spring force to the walls to reproduce the real physical process of atoms in the microscopic level to ensure the stability of the model during the simulation process, and the spring constant is set to k=70 N/m. The dimensions of the computational model are given in Table 1.

Table 1 Dimensions of the flow heat transfer model

Length (L_x)	Width (L_y)	Height (L_z)	Top thickness (D_{top})	Bottom thickness (D_{bottom})	Channel height (H)
32 a_0	10 a_0	20 a_0	4 a_0	6 a_0	10 a_0

The top and bottom solid surfaces are assumed to be infinite planes in the simulations, so periodic boundaries are used in the x and y directions of the model to simulate an infinitely extended space. However, due to the existence of temperature-controlled area and the external force application region in the x-direction, the periodic boundary in this direction is slightly different from the classical periodic boundary, which can be called the class periodic boundary. z-direction adopts the fixed boundary to maintain the stability of the structure.

2.2 Potential function and related parameter settings

The interactions between atoms in the simulated system are calculated by means of a mixing potential function, which consists of two parts: the LJ potential and the long-range Coulomb force. The calculated energy parameters of the LJ potential function are given in Table 2. The long-range Coulomb force and the LJ potential function have a truncation distance $r_{c1}=r_{c2}=10$ Å. The interaction parameters between solids and liquids are calculated using the L-B mixing rule [18] (Eq. (1) and Eq. (2)). The interaction parameters between O-Cu are obtained from the interaction parameters between O-O and Cu-Cu. Since the SHAKE algorithm is used for the water molecule in the simulation, which is considered as a rigid body, and the interaction forces of the hydrogen atoms do not have a significant effect on the results of the simulation [19], the interactions between the hydrogen atoms are not taken into account in the simulation. The rules for calculating the interaction between solids and liquids are described below:

$$\sigma_{sl} = \frac{\sigma_{ss} + \sigma_{ll}}{2} \tag{1}$$

$$\varepsilon_{sl} = \sqrt{\varepsilon_{ss} \times \varepsilon_{ll}} \tag{2}$$

Table 2 Information on the molecular interaction parameters

Interaction	σ (Å)	ε (J)
Pt-Pt	2.475	8.35×10^{-20}
Ar-Ar	3.405	1.67×10^{-21}

The molecular interaction parameters derived from the L-B mixing rule are listed in Table 3. [20]

Table 3 Information on the molecular interaction parameters

Interaction	σ (Å)	ε (ev)	q(e)
H-H	0	0	0.4238
O-O	3.166	6.739×10^{-3}	-0.8476
O-Cu	2.751	7.372×10^{-3}	

In this simulation, the convective heat transfer performance between the argon fluid and the cold and hot wall surfaces of the flow channel is investigated under the conditions of different electric field strengths *E* and ion concentration *C*. For the convenience of subsequent statistical calculations, the ion concentration in the *Ar* solution is defined as the ratio of the number of ions in the solution to the number of solvent atoms in the solution, and the calculation formula is as follows:

$$C = \frac{N_{iron}}{N_{Ar}} \tag{3}$$

Where *C* is the concentration of positive/negative ions in the solution, which is a dimensionless number. N_{iron} is the number of positive/negative ions in the solution, and N_{Ar} is the number of Ar atoms in the solution.

2.3 Model validation

To ensure the accuracy and reliability of the calculation results, the model is validated using the thermal conductivity of argon fluid prior to calculation. The NEMD method is used to simulate the thermal conductivity of argon fluid at standard atmospheric pressure of 300K, and the results are compared with standard data published by the National Institute of Standards and Technology (NIST) in the United States. In the calculation, the heat flux and temperature distribution obtained from the heat flux calculation are used to calculate the thermal conductivity of argon fluid using Fourier's fundamental law of thermal conductivity as shown in Eq. (4).

$$\lambda = -\frac{\Phi}{A\left(\frac{\partial T}{\partial x}\right)} \tag{4}$$

In the formula, *Φ* is the heat flux, *A* is the cross-sectional region of heat conduction, $\partial T / \partial x$ is the temperature gradient along the direction of heat transfer. As shown in Table 4, the results calculated by the validation model are relatively close to the data in NIST, proving the reliability of the molecular dynamics calculation model in this paper.

Table 4 Dimensions of the flow heat transfer model

$T(K)$	$\lambda(W/(m \cdot K))$ (**calculated**)	$\lambda(W/(m \cdot K))$ (**NIST**)	**deviation**
300K	0.01592	0.01772	10.15%

3. RESULTS AND DISCUSSION

3.1 The influence of electric field strength on heat flow control

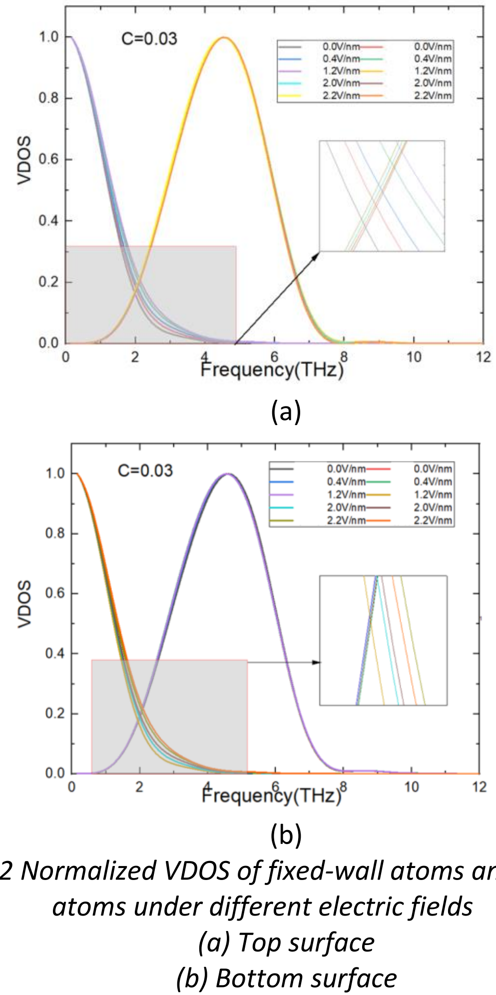

(a)

(b)

Fig. 2 Normalized VDOS of fixed-wall atoms and fluid atoms under different electric fields

(a) Top surface

(b) Bottom surface

In order to investigate the effect of electric field strength on the heat transfer characteristics of the flow channel, the concentration of ions *C* is set to 0.03 and the electric field strength *E* is varied from 0.0 V/nm to 2.2 V/nm. Fig. 2 shows the comparison of the VDOS of the stationary fixed-wall atoms with that of the fluid atoms for different electric field strengths. It can be seen that the VDOS overlap area of both the top and bottom atoms with the fluid atoms increases as the electric field strength increases. The VDOS overlap area between atoms on the top and atoms in the fluid increases by 17%, 30%, 47%, and 55% for values of the electric field strength *E* of 0.4 V/nm, 1.2 V/nm, 2.0 V/nm, and 2.2 V/nm, respectively, compared to that in the absence of an applied electric field. The area of VDOS overlap between the atoms of the bottom surface and the fluid atoms also increases with the increase of the electric field strength, up to 56% according to Fig. 3. This change indicates that the heat transfer efficiency of both the top

and bottom surfaces is enhanced by the electric field, a phenomenon that may originate from the effect of the electric field on the frequency distribution of the phonon vibrations. The increase in the electric field strength changes the degree of coupling between the wall atoms and the fluid atoms, which affects the heat transfer efficiency between the interfaces. Specifically, the applied electric field leads to an increase in coupling between the solid and fluid atoms, and the degree of increase increases with the increase in electric field strength, with the increase in coupling between the top and fluid atoms being slightly weaker than that between the bottom and fluid atoms. This indicates that the increase in electric field strength leads to a decrease in the interfacial thermal resistance between the top and bottom surfaces and the fluid, where the decrease in interfacial thermal resistance on the top surface is slightly smaller than that on the bottom surface.

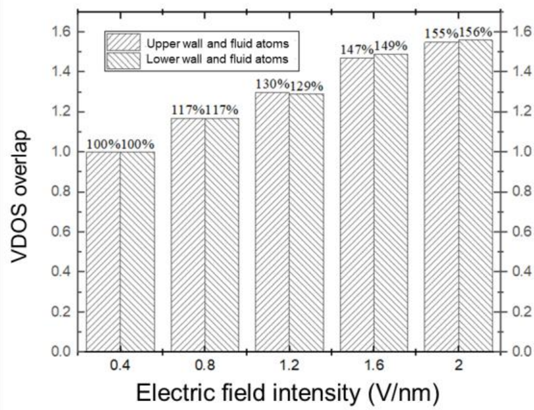

Fig. 3 VDOS overlap of fixed-wall and fluid atoms at different electric field strengths

Fig. 4 shows the cloud view of the temperature distribution of the fluid in the microchannel under different electric field strengths. As the electric field strength increases, the high temperature region of the field in the channel is more skewed towards the bottom surface, and the low temperature region near the top surface increases. Fig. 5 shows the temperature distribution of the fluid along the x-direction at different electric field strengths, and the average temperature of the fluid in the channel increases slightly with the increase of the electric field strength, and the temperature increase increases after the fluid flows through the channel. When the electric field strength is 2.0 V/nm, the temperature difference between the inlet and outlet of the fluid increases by 22.4% compared to that in the absence of electric field. The increase in the average fluid temperature and the increase in the temperature difference between the fluid inlet and outlet with the increasing electric field strength indicate. On the one hand, the heat dissipation at the bottom surface increases by increasing the electric field strength and, on the other hand, the increase in the electric field strength increases the percentage of the heat carried away by the fluid and decreases the percentage of the heat dissipated to the environment through the top wall.

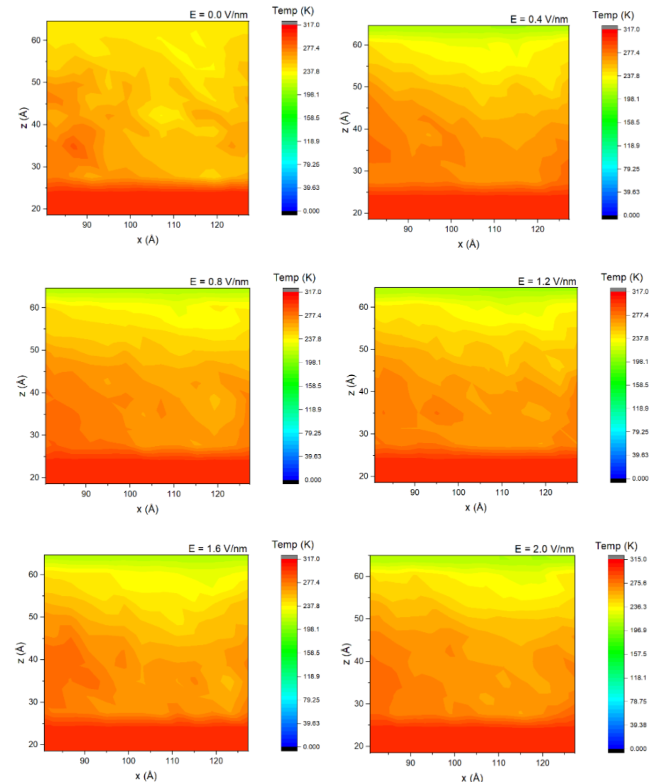

Fig. 4 Temperature clouds of the channel at different electric field strengths

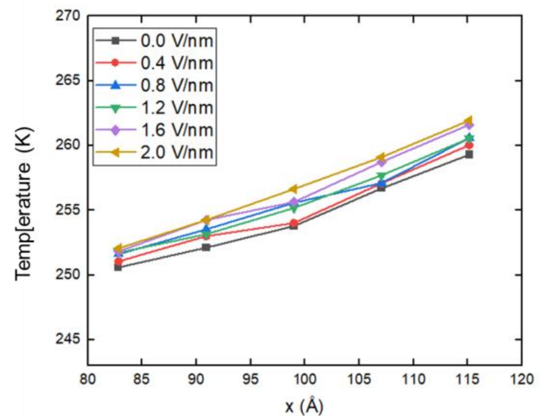

Fig. 5 Temperature distribution in the x-direction of the channel for different electric field strengths

Fig. 6 shows the changes in the heat flux density on the top and bottom surfaces when different levels of field strength are applied to the system, and it can also be seen that the heat flux density on both the top and bottom surfaces increases with the increase in the electric field strength, but the increase in the heat flux

density on the bottom surface is relatively large, whereas the top surface is slightly increased. This is mainly a result of the change in the flow rate of the fluid near the top and bottom surfaces caused by the electric field strength.

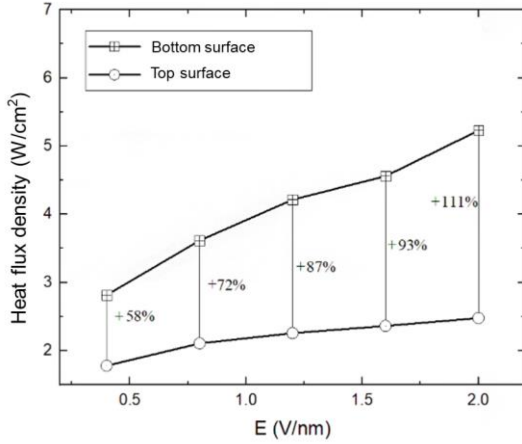

Fig. 6 Heat flow density at the wall for different electric field strengths

Fig. 7 shows the localized average *Nu* changes near the top and bottom surfaces at different electric field strengths. It can be seen from Fig. 7(a) that the Nu_x at the top surface has a small change along the flow direction; however, with the increase of the electric field strength Nu_x increases slightly. The Nu_x on the bottom shows a decreasing and then increasing trend along the flow direction. With the increase of the electric field strength Nu_x shows an overall increasing trend. Compared with the top, the value of Nu_x on the bottom is larger. This indicates that the influence of electric field strength on the bottom is more significant

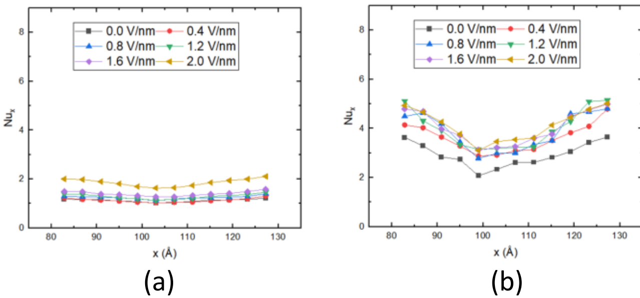

Fig. 7 Nu_x along the top and bottom surface at different electric field strengths

(a) Nu_x along the top surface

(b) Nu_x along the bottom surface

3.2 Analysis of heat flux

Fig. 8(a) shows the normalized heat flux of the fluid along the x-direction at different electric field strengths, The heat flux of the fluid along the x-direction increases with the increase in electric field strength. Fig. 8(b) shows the dimensionless heat flux of the fluid along the z-direction (perpendicular to the interface direction) with different electric field strengths, and the heat flux along the z-direction increases with the increase in electric field strength. Comparing the result in the two graphs, the increase of heat flux along the x-direction is substantially higher than the increase of heat flux along the z-direction. Fig. 9 compares the dimensionless heat in both directions for different electric field strengths.

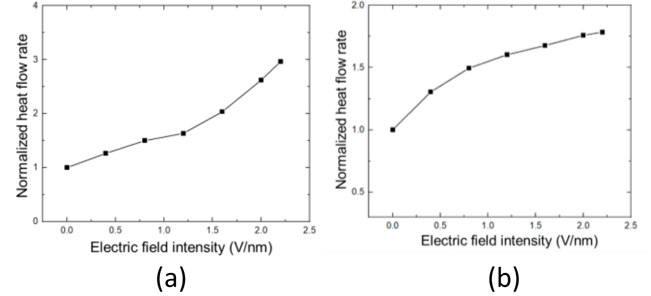

Fig. 8 Normalized heat flux of fluid for different electric field strengths

(a) Normalized heat flux along the x *direction*

(b) Normalized heat flux along the z *direction*

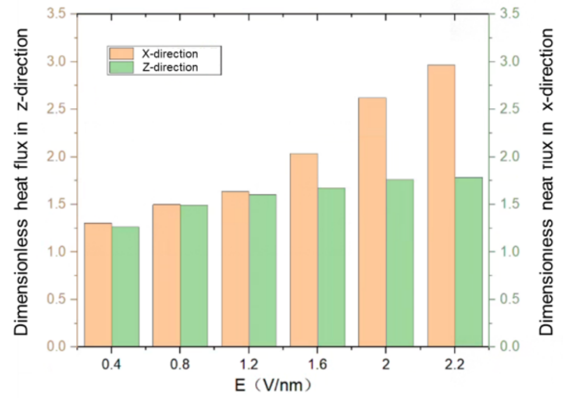

Fig. 9 Comparison of normalized dimensionless heat fluxes

Fig. 10 shows the temperature of the outer wall of the model as different electric field strengths are applied to the flow channel. The temperature of the outer surface of the model decreases as the electric field strength increases, indicating that the increasing of electric field strength can effectively reduce the outer surface temperature of the system. That is, increasing the electric field strength can realize the modulation effect of heat flow, so that the heat on the wall surface is carried away by the fluid as much as possible. In the range of electric field strengths studied, the trend of decreasing the temperature of the outer wall surface slows down when the electric field strength is greater than 1.2 V/nm, and the final value of the outer temperature stabilizes around 101.5 K. The temperature of the outer wall surface decreases when the electric field strength is greater than 1.2 V/nm. The temperature

of the outer surface of the channel decreases by 109.2 K when an electric field of 2.2 V/nm is applied, compared to that without an electric field, so increasing the electric field can effectively reduce the temperature of the outer surface of the system.

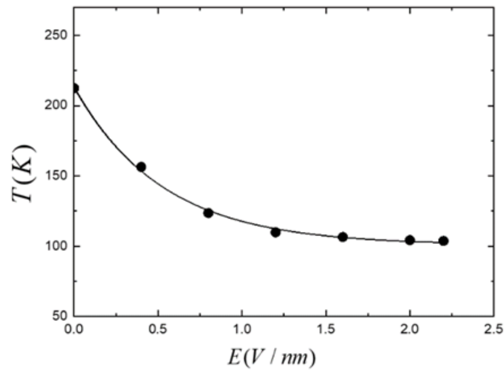

Fig. 10 Temperature of the outer layer of the model for different electric field strengths

4. CONCLUSIONS

This study proposes a model for the influence of electric field strength on heat transfer in flow channels, which includes model configuration, potential function selection, solver optimization and temperature control strategy. The following conclusions are drawn by exploring the effect of electric field strength on heat transfer in platinum-argon atomic flow channels:

(1) With the increase of electric field strength, the spatial distribution of the fluid atoms becomes closer, which improves the heat transfer performance of the fluid.

(2) The increase of electric field strength also enhances the coupling degree between the top and bottom surfaces and the fluid atoms at the same time, in which the VDOS overlap area between the top and bottom atoms and the fluid atoms increases by 55% and 56%, respectively, compared with that in the case of no applied electric field, indicating that the increase of electric field strength enhances the heat transfer efficiency between the wall surfaces and the fluid.

(3) Increasing the electric field strength improves the convective heat transfer characteristics in the microchannel. Compared with no electric field, the Nu of the bottom and the top surfaces increased by 42% and 56%, respectively, and the temperature difference between the inlet and outlet of the fluid increased by 22.4%, and the temperature of the outside decreased by 109.2 K at an electric field strength of 2.0 V/nm.

REFERENCE

[1] R. Hu, W. Xi, Y. Liu, et al., Thermal camouflage metamaterials [J], Mater. Today 45 (2021) 120-141.

[2] C. Xu, C. Liu, G. Fang, et al., Design, preparation and performance evaluation of core unit in multispectral camouflage coating[J], Infrared Phys. Technol. 121 (2022), 104013.

[3] H.L. Dong, J.C. Wang, Y.R. Zeng, et al., Reflection spectrum study of THz wave by infrared low emissivity stealth coating[J], Spectrosc. Spectr. Anal. 39 (10) (2019) 3007-3012.

[4] J. Jian, X. Wang, L. Li, et al., Continuous tuning of phase transition temperature in VO2 thin films on c-cut sapphire substrates via strain variation[J], ACS Appl.Mater. Interfaces 9 (6) (2017) 5319-5327.

[5] Y. Zhao, X. Zhang, X. Chen, et al., Preparation of WO3 films with controllable crystallinity for improved near-infrared electrochromic performances[J], ACS Sustain. Chem. Eng. 8 (31) (2020) 11658-11666.

[6] L. Peng, D. Liu, H. Cheng, et al., A multilayer film based selective thermal emitter for infrared stealth technology[J], Adv. Opt. Mater. 6 (23) (2018), 1801006.

[7] J.L. Niu, Y. Wang, X.L. Zou, et al., Infrared electrochromic materials, devices and applications[J], Appl. Mater. Today 24 (2021), 101073.

[8] B. Wang, G. Xu, S. Song, et al., Flexible, infrared adjustable, thermal radiation control device based on electro-emissive PANI/Ce(4+)thin films inspired by chameleon[J], Chem. Eng. J. 445 (2022), 136819.

[9] M. Pan, Y. Huang, Q. Li, et al., Multi-band middle-infrared-compatible camouflage with thermal management via simple photonic structures[J], Nano Energy 69 (2020), 104449.

[10] M. Zhang, S. Li, Low-cost and facile implementation of microfluidic colour-changing devices using dry film photoresist-based moulds[J], J. Exp. Nanosci. 13 (1) (2018) 220-229.

[11] R. van Erp, R. Soleimanzadeh, L. Nela, et al., Co-designing electronics with microfluidics for more sustainable cooling[J], Nature 585 (7824) (2020) 211-216.

[12] Harikrishna H, Ducker W A, Huxtable S T. The influence of interface bonding on thermal transport through solid-liquid interfaces[J]. APPLIED PHYSICS LETTERS, 2013,102(25).

[13] Barrat, Jean-Louis and François Chiaruttini. “Kapitza resistance at the liquid—solid interface.” [J] Molecular Physics 101 (2002): 1605 - 1610.

[14] L. Xue, P. Keblinski, S. R. Phillpot, S. U.-S. Choi, J. A. Eastman; Two regimes of thermal resistance at a liquid–solid interface[J]. J. Chem. Phys. 1 January 2003; 118 (1): 337–339.

[15] Bo Hung Kim, Ali Beskok, Tahir Cagin; Molecular dynamics simulations of thermal resistance at the liquid-

solid interface[J]. J. Chem. Phys. 7 November 2008; 129 (17): 174701.
[16] Sohail Murad, Ishwar K. Puri; Thermal transport across nanoscale solid-fluid interfaces[J]. Appl. Phys. Lett. 31 March 2008; 92 (13): 133105.
[17] Ma, Y., et al., Ordered water layers by interfacial charge decoration leading to an ultra-low Kapitza resistance between graphene and water[J]. Carbon, 2018. 135: p. 263-269.
[18] Johnson R A. Analytic nearest-neighbor model for fcc metals[J]. Physical Review B, 1988,37(8):3924-3931.
[19] Evans W, Fish J, Keblinski P. Thermal conductivity of ordered molecular water[J]. JOURNAL OF CHEMICAL PHYSICS, 2007,126(15).
[20] Allen M P, Tildesley D J. Computer Simulation of Liquids[Z]. Oxford University Press, 2017.